

# Realtime Selection of Optimal Source Parameters Using Ground Motion Envelopes

Dario Jozinović \*, John Clinton <sup>1</sup>, Frédéric Massin <sup>1</sup>, Maren Böse <sup>1</sup>, Carlo Cauzzi <sup>1</sup>

<sup>1</sup>Swiss Seismological Service, ETH Zurich, Zurich, Switzerland

**Author contributions:** *Conceptualization:* JC, DJ. *Data Curation:* DJ, FM, CC. *Methodology:* DJ, JC, FM, MB. *Formal Analysis:* DJ. *Investigation:* DJ. *Writing - original draft:* DJ, JC, FM, MB. *Writing - Review & Editing:* DJ, JC, FM, MB, CC. *Visualization:* DJ, FrM. *Supervision:* JC.

**Abstract** It is increasingly common for seismic networks to operate multiple independent automatic algorithms to characterise earthquakes in real-time, such as in earthquake early warning (EEW) or even standard network practice. Commonly used methods to select the best solution at a given time are simple and use ad hoc rules. An absolute measure of how well a solution (event origin and magnitude) matches the observations by the goodness-of-fit between the observed and predicted envelopes is a robust and independent metric to select optimal solutions. We propose such a measure that is calculated as a combination of amplitude and cross-correlation fit. This metric can be used to determine when a preferred solution reaches an appropriate confidence level for alerting, or indeed to compare two (or more) different event characterisations directly. We demonstrate that our approach can also be used to suppress false alarms commonly seen at seismic networks. Tests using the 10 largest earthquakes in Switzerland between 2013 and 2020, and events that caused false alarms demonstrate that our approach can effectively prefer solutions with small errors in location and magnitude, and can clearly identify and discard false origins or incorrect magnitudes, at all time scales, starting with the first event characterisation.

Production Editor:  
Gareth Funning  
Handling Editor:  
Andrea Llenos  
Copy & Layout Editor:  
Théa Ragon

Received:  
October 10, 2023  
Accepted:  
April 22, 2024  
Published:  
May 9, 2024

## 1 Introduction

Over recent decades, earthquake early warning (EEW) algorithms have been continuously developed and EEW systems have become operational in many regions around the world (e.g. Cremen and Galasso, 2020; Allen and Melgar, 2019; Clinton et al., 2016). The goal of EEW is to rapidly estimate developing ground shaking from an ongoing earthquake at a specific location or region, thus providing users with the opportunity to take action before strong ground motions arrive and hence minimise the impact of the shaking.

The Swiss Seismological Service (SED) at Eidgenössische Technische Hochschule (ETH) Zurich has been actively engaged in the development and implementation of EEW algorithms for over a decade (e.g. Massin et al., 2021; Behr et al., 2016), including the Virtual Seismologist (VS; Cua, 2005; Cua and Heaton, 2007) and Finite-Fault Rupture Detector (FinDer; Böse et al., 2012, 2015, 2018, 2023) algorithms. Operationally, these algorithms are integrated as modules within the earthquake monitoring platform SeisComP - a technical framework named the ETHZ-SED SeisComP EEW system (ESE; Massin et al., 2021). Both of these algorithms estimate the earthquake source parameters (location and magnitude) which are then used to estimate ground shaking at a set of locations or a region. In the current implementation, the VS algorithm provides a predictive magnitude, based on the recorded amplitudes and rapid point-source earthquake location provided through ex-

isting SeisComP modules. FinDer provides an estimate of the best-fitting line-source model by comparing the peak ground acceleration (PGA) values at stations to a set of pre-generated templates. Both algorithms provide independent estimates of the earthquake source parameters. Differences in their performance during an earthquake can arise from the properties of the seismic source (magnitude, source complexity); the network geometry; the data quality (e.g. both algorithms are sensitive to spikes and metadata errors), and contemporary seismicity. A system building on multiple independent algorithms, like ESE, is more robust and tolerant to failure (Massin et al., 2021).

Like the majority of seismic networks, the SED also uses the SeisComP framework for routine automated monitoring, and also operates a suite of automatic detectors (simple STA/LTA and post-detectors) and locators (scautoloc and scanloc) that target different types of seismicity and use different velocity models. Further, as more and more stations trigger, each ‘pipeline’ produces updated origins. This means that for an ongoing, even moderate event, the automatic system provides a highly dynamic output with many tens of different origins. Providing solutions from a few stations allows small events to be identified and the earliest solutions for large events. Allowing frequent updates as more phase picks arrive means better accuracy can be achieved as the energy from the seismic event progresses across the seismic network

However, having multiple source parameter solutions requires a method capable of preferring or combining

\*Corresponding author: dario.jozinovic@sed.ethz.ch

them. At the SED, we currently use a location score based only on origin parameters (such as number of picks, azimuthal gap, etc.), that does not take magnitude into account. Other approaches are available, for example by simply using a weighted average of the solution parameters (Kohler et al., 2020). Minson et al. (2017) propose a more complex approach in which a constrained least squares fit between observed and predicted acceleration waveform envelopes from all the stations in the network is calculated. This is done for each algorithm solution and used to estimate the relative probability for single solutions or their combinations being correct, with the sum of the probabilities summing to 1. Furthermore, a ‘no event’ solution, for which the predicted envelopes are equal to zero, is used to obtain the probability of no earthquake existing, corresponding to a false alarm. The method allows the preference or combination of the ground motion predictions according to the relative probabilities assigned. However, it does not provide a measure for the quality of a solution, only its relative quality compared to other possible solutions.

Motivated by the approach of Minson et al. (2017), in this study we also compare the observed and predicted envelopes. We employ the same envelope functions (Cua, 2005) with appropriate adjustments to Switzerland (see the Electronic Supplement to this article). However, instead of calculating the *relative* probabilities of solutions from the given algorithms being correct, we provide an *absolute* goodness-of-fit measure associated with each source parameter estimate, which can then be used to select the preferred solution (i.e. the location, magnitude and origin time) and to check if this solution reaches a pre-defined threshold for alerting. Also, instead of a least squares fit between the observed and predicted envelopes, our approach uses the combination of amplitude fit and cross-correlation between the envelopes, requiring that amplitude and shape fit well but allowing for some timing error, for example in the velocity model. We also do not set the noise level of the predicted envelopes to zero but to the median noise level at the stations used in this study.

Our approach can be implemented in EEW systems as well as in general seismic observatory practice. It can be used to compare multiple available automated seismic solutions, irrespective of the source algorithm and model, and to provide a preferred origin and magnitude. Crucially, it can also be used to compare both point-source (as provided by standard SeisComP locators) and finite-source (as provided by FinDer) solutions, since it can support different distance metrics, including hypocentral or rupture distances.

We test our method on a set of earthquakes and false alarms that occurred in real-time processing at the SED since 2013. The algorithm can successfully prefer source parameter estimates that are close to the network solution with both early solutions including only seconds of data at closest stations, as well as using the full data from a large network. We find it is particularly effective in suppressing processing blunders from significant errors in automated locations or significantly elevated magnitudes that are regular issues in seismic

network monitoring.

## 2 Methods

Our proposed method is based on the comparison of observed and predicted velocity waveform envelopes (Fig. 1) at a set of seismic stations. We obtain the observed earthquake envelopes (following the approach of Cua, 2005), computed by the *sceewenv* SeisComP module (Massin et al., 2021), which provides continuous real-time streams of envelope values (Behr et al., 2016). Envelope computation in *sceewenv* involves the following sequential steps: correct for the gain and baseline offset and check for a clipped signal (neglecting the sensor if has a saturated signal); compute the root-mean-square of the two horizontal components to obtain a single combined horizontal component, integrate to velocity (if needed); apply a 4th order Butterworth high pass filter with a corner frequency of 3 s; and, compute the maximum absolute amplitude within 1 s intervals.

We calculate the predicted envelopes following the Cua (2005) relationship, using magnitude, hypocentral distance and site class (either “rock” or “soil”). To attribute the site class to the stations used in this study, when available, we used the EC8 ground types (Eurocode 8, 2005) available from the SED stations website (Swiss Seismological Service At ETH Zurich, 1983). EC8 ground types are categorised as rock for EC8 ground types A and B) or soil for all other EC8 ground types and as default in the absence of EC8 type. The relationship then outputs P and S waveform envelopes, which start at earthquake origin time with a specified duration that matches the time window of the available station waveform. The Cua (2005) predicted envelopes were calibrated using data from southern California, which consisted of about 30,000 records (vertical and horizontal acceleration, velocity, and displacement) from 70 southern California earthquakes ( $2 \leq M \leq 7.3$ ) recorded within 200 km from the earthquake source. However, for the subset of Swiss earthquakes we used, we observed (Figure S7 in the electronic supplement) that these predicted envelopes often do not fit the observed shaking well and visual checks showed a systematic overpredicting of the observed shaking. Therefore we decided to scale the predicted envelopes using the GMM developed by Cauzzi et al. (2015) for Switzerland (see also Edwards and Fäh, 2013). This approach reduced the difference in peaks between observed and predicted envelopes (Figure S7 in the electronic supplement). While this significantly improved the overall envelope fit, we still found that the maxima of the P-waves (especially at the closest stations) were higher in the observed data. We then further adapted the predicted envelopes using a station-specific S-P scaling and multiplication of the P-wave amplitude with an ad-hoc scaling factor. Further details are given in the Electronic Supplement.

We then compute the goodness-of-fit,  $G$ , of the observed and predicted (parts of the) waveform envelopes for each station  $S$  at time  $t$  as

$$G(S, t) = 100 \cdot \sqrt{A(S, t) \cdot C(S, t)} \quad (1)$$

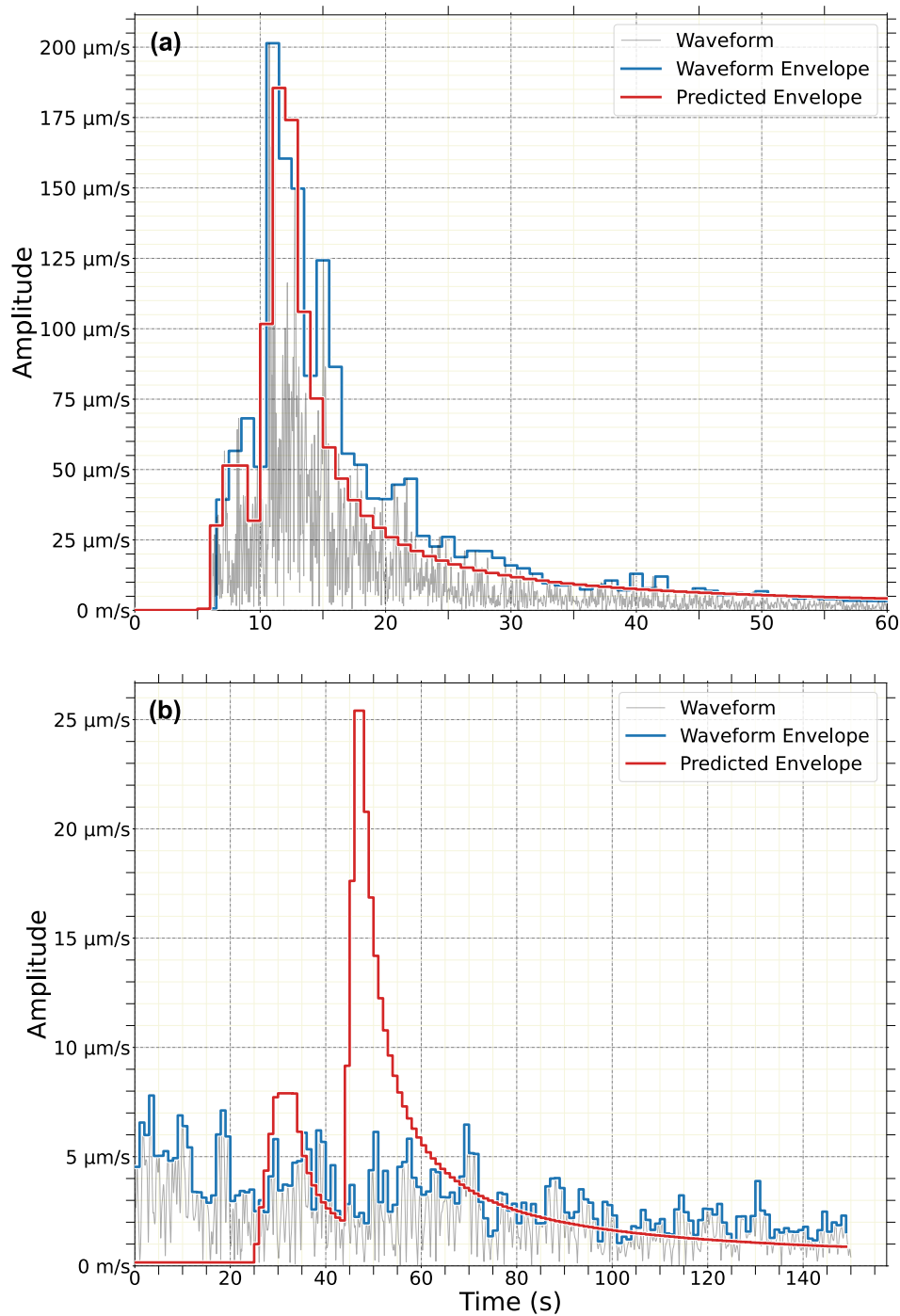


**Figure 1** Comparison between true (with accompanying waveform) and predicted envelopes for (a) an earthquake and (b) a false alarm. The subplot a) shows the comparison for an event of M 3.5 at a station 31 km from the hypocentre. The subplot b) shows the comparison for a false M 3.5 at 151 km hypocentral distance, caused by a teleseismic earthquake (M 8.2 in Mexico)

where  $A(S, t)$  is the amplitude fit, and  $C(S, t)$  is the normalised zero-shift cross-correlation between the observed and predicted envelopes that start at time  $t_0$  and end at time  $t$ , where  $t_0$  can be an arbitrarily defined envelope start time (e.g. earthquake origin time, P-arrival at the closest station, etc.). The amplitude fit,  $A(S, t)$ , is calculated as

$$A(S, t) = 1 - \left( \frac{o(S, t) - m(S, t)}{o(S, t) + m(S, t)} \right)^2 \quad (2)$$

where  $o(S, t)$  and  $m(S, t)$  are the peak amplitudes of the observed and predicted envelope at time  $t$ , respec-

tively. We decided to compare only the maxima of the observed and predicted envelopes as we are modelling the difference in envelope shapes using the cross-correlation fit,  $C(S, t)$ , calculated as

$$C(S, t) = \frac{\sum_{i=1}^n O(S, t)_i M(S, t)_i}{\sqrt{\sum_{i=1}^n O(S, t)_i^2} \sqrt{\sum_{i=1}^n M(S, t)_i^2}} \quad (3)$$

where  $O(S, t)$  and  $M(S, t)$  are observed and predicted envelopes at time  $t$ , respectively, and  $n$  is the number of samples (seconds) in the envelope. While using  $C(S, t)$  increases the processing time of our algorithm (which

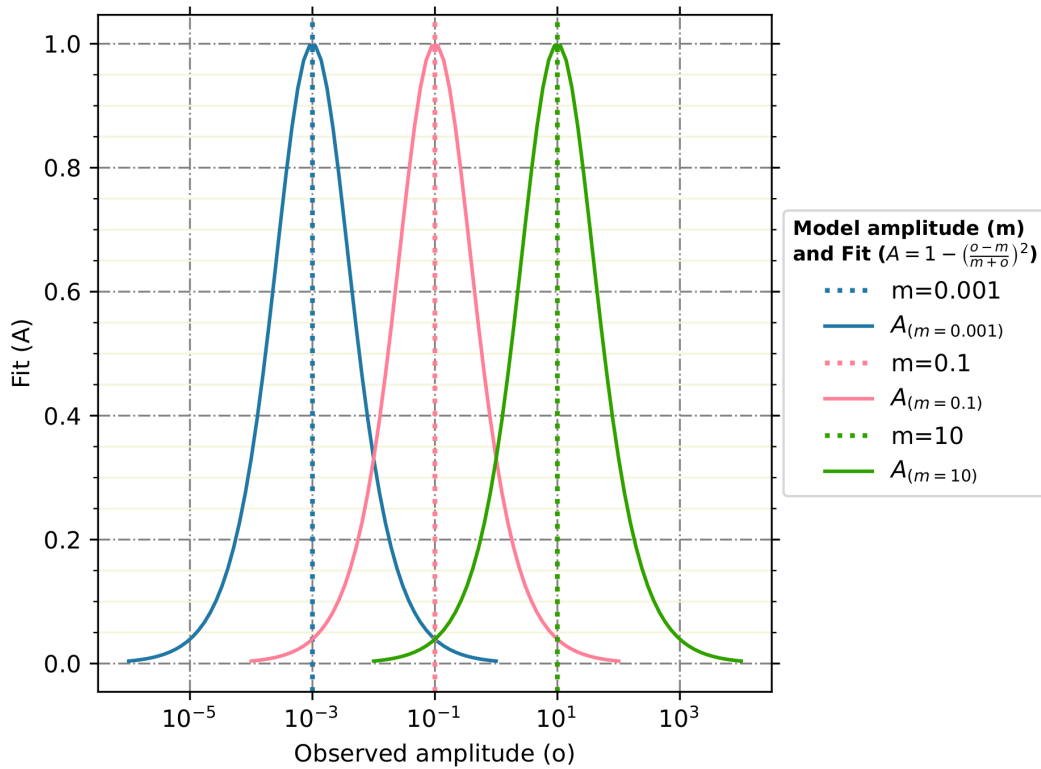


**Figure 2** The amplitude fit function  $A(S, t)$  in equation 2. The curves show the value of the fit, depending on the difference between the observed ( $o$ ) and predicted ( $m$ ) peak values. The predicted values are fixed (dotted vertical line) for 3 different values (3 colours). The amplitude fit  $A$  is shown for different observed amplitudes for each of the 3 fixed predicted values. Note that the shape of  $A$  is scale-invariant on a log scale.

still remains insignificant), it allows us to address possible (unrealistically) good amplitude fits for certain combinations of both wrong magnitude and distance that can produce similar amplitude maxima as the observed data (e.g. for an M 5.5 earthquake at 50 km distance the predicted PGV is 0.0054 m/s and for an M 5 earthquake at 25 km distance the predicted PGV is 0.0055 m/s), but can be easily discriminated by the envelope shape.

The functional form of  $A(S, t)$  in equation 2 was chosen because of its symmetric fit with exponential decay (Fig. 2) as a function of the difference between  $o(S, t)$  and  $m(S, t)$ . Furthermore, we opted to use the functional form of  $A(S, t)$  in equation 2 over a least-squares-fit as used in Minson et al. (2017) because the value of  $A(S, t)$  is bounded between 0 and 1 and depends on relative differences in predicted and observed amplitudes rather than absolute values (i.e. larger amplitudes do not affect the fit disproportionately). Crucially, this produces a bounded absolute fit measure that is independent of earthquake size, allowing us to prefer the best magnitude and location estimate (although it systematically penalises weaker motions - for example for an observed ground motion of 2 mm/s, predicted ground motions 1 mm/s and 4 mm/s both provide the same  $A(S, t)$  value).

Finally, the mean goodness-of-fit across all included stations at time  $t$  is calculated and used as the measure of the goodness-of-fit for the given source parameters. The same procedure is applied again for both existing and new source parameter estimates as more and more data arrives from already included and newly in-

roduced stations - resulting in a goodness-of-fit metric that evolves over time. We then choose the solution with the highest mean goodness-of-fit, i.e. that best fits the observed ground motions, as our preferred solution.

In practice, at any given time  $t$ , we only use stations where the predicted or observed earthquake ground-motion envelopes are non-zero - that is those stations within a certain distance, dependent on time  $t$ , from the hypocenter (or rupture plane). The duration of the predicted envelope matches the available data from the observed stations at time  $t$ . In this manner, the method can account for differing data latencies from seismic stations if operated in real-time. A further benefit of this approach is that it reduces processing time and does not allow the fit between observed and predicted noise (which is hard to model, and is station or sensor specific) to affect the final goodness-of-fit measure.

### 3 Data

We evaluate the performance of the proposed algorithm in two separate tests using data collected by the Swiss seismic network. This first is a retrospective analysis using recent moderate earthquakes. The second test analyses a set of significant false earthquake alerts that were produced in recent years. We explore both (1) how sensitive our method is at identifying differences in location and magnitudes, and (2) how effective it is at identifying false alarms. All tests are performed using different window lengths after the P-wave arrival at the clos-

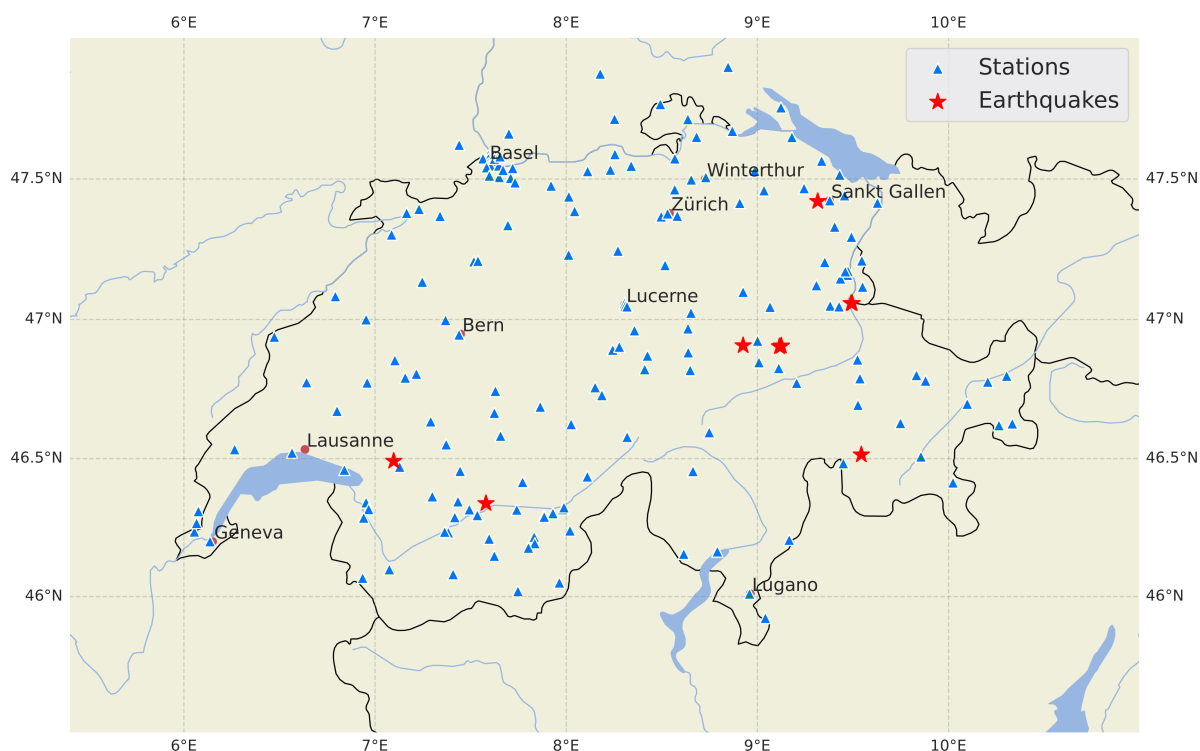


**Figure 3** Map of the stations (network codes CH, C4) and the 10 Swiss earthquakes (Table 1 for details of the events) used in the analysis. Some earthquakes have very similar locations, so their markers overlap on the map.

Date (UTC)	Latitude (°N)	Longitude (°E)	Magnitude (M <sub>lh</sub> )	Depth (km)
2020-11-10 T 12:53	46.9	9.12	3.9	1.7
2020-10-25 T 19:43	46.9	9.12	4.3	1.4
2020-10-25 T 19:35	46.91	9.12	3.6	1.4
2017-07-01 T 08:10	46.49	7.1	4.3	4.3
2017-03-06 T 20:12	46.91	8.93	4.6	4.2
2016-10-24 T 14:44	46.34	7.58	4.1	8.2
2016-10-07 T 07:27	46.51	9.54	3.8	10
2013-12-27 T 07:08	47.06	9.5	3.7	6.2
2013-12-12 T 00:59	47.06	9.49	4.1	5.9
2013-07-20 T 03:30	47.42	9.32	3.5	4.5

**Table 1** Earthquakes used in this study.

est station, ranging from  $t=1$  s to  $t=40$  s. We conduct our tests using the earthquakes and stations located in Switzerland, a sufficiently small region for which 40 s long waveforms provide enough input data to our algorithm. The sample of recent earthquakes includes the ten largest events that occurred in Switzerland between 2013 and 2020 (Table 1; Fig. 3), with events magnitudes ranging from 3.5 to 4.6 and depths of 1.4 to 10 km.

The sample of 20 false alarms (Table 2) comprises real events (quarry blasts and regional or teleseismic earthquakes) and non-existing events (i.e. noise bursts), that were assigned wrong (or any in case of non-existing events) locations and magnitudes due to combinations of false triggers during routine monitoring. These events typically were released to the public (e.g. on social media platforms) by the alerting system at the Swiss Seismic Network. Alerts are released for automatic solutions with  $M > 2.5$  and an epicenter lying inside or close

to Switzerland that reach the quality threshold based on the SED 'location score'. Currently, solutions (including false alarms) are generated using the scautopick module in SeisCompP, using a minimum of 6 associated picks. The SED 'location score' (Diehl et al., 2015) takes into account the distribution of pick residuals, location azimuthal gap, location RMS, and the number of arrivals used for location.

We obtain the earthquake and station metadata from the ETHZ dataset in the SeisBench package (Woollam et al., 2022). The ETHZ dataset is derived from 1) the National Earthquake Catalogue of Switzerland (see Data and Resources section) for earthquake information; and 2) the ETH EIDA node for seismic waveform data and metadata. Seismic stations used are from network code CH (Swiss Seismological Service At ETH Zurich, 1983) and C4 (C.E.R.N., 2016), comprising 178 stations. See Figure 3 for stations and events. The false

Real event	Date	False Latitude (°N)	False Longitude (°E)	False magnitude	False depth (km)
Quarry Blast (M=1.6) 46 km from false alarm location	12.06.2019	47.09	7.53	2.8	39.9
Quarry Blast (M=1.5) 140 km from false alarm location	26.08.2020	47.14	9.01	2.8	10
Quarry Blast (M=2) 0 km from false location	1.10.2020	47.53	8.18	2.5	6.4
Quarry Blast (M=1.7) 38 km from false location	5.11.2020	47.31	7.81	2.6	37.7
Quarry Blast (M=0.9) 105 km from false location	01.07.2022	47.17	7.19	2.9	10
M6.4 in Crete, Greece, 1584 km from false location	12.10.2013	46.72	11.46	3.6	12.3
M5.2 in Greece, 1274 km from false location	30.03.2019	46.37	11.21	3.1	27.8
M5.2 in Greece, 2042 km from false location	30.01.2020	46.83	8.94	2.6	76.2
M5.3 in Crete, Greece, 1993 km from false location	23.05.2020	46.53	8.35	2.6	54.4
M5.4 event in Greece, 1664 km from false location	18.12.2021	46.06	8.27	2.6	27.4
M5.1 event in southern Italy, 916 km from false location	31.10.2022	46	8.19	2.8	3.6
M7.9 in Papua New Guinea, 119° from false location	22.01.2017	46.97	10.31	3.3	61.2
M8.2 in Chiapas, Mexico, 90° from false location	08.09.2017	46.38	11.78	3.5	22.8
M6.8 in Fiji, 151° from false location	18.11.2018	46.78	8.84	2.8	58.1
M7.1 in Anchorage, Alaska, 71° from false location	30.11.2018	46.35	10.18	3.6	3
M6.7 in Fiji, 152° from false location	01.09.2019	46.69	9.57	2.7	36.5
Non-existing event	11.01.2019	44.82	8.13	3.7	27.6
Non-existing event	05.07.2019	46.54	9.38	3.2	10
M3.6 event, 115 km from false location	25.10.2020	47.48	7.85	2.7	5.9
M3.7 event in Albstadt, Germany, 248 km from false location	21.03.2021	46.51	6.9	2.5	28.5

**Table 2** False alarms used in this study.

alarms are representative examples collected from the operational experience during past years.

The observed earthquake envelopes have been calculated by the *sceewenv* module in SeisComp, as described in the Methods 2 section. We calculate the predicted envelopes following the Cua (2005) relationship (details explained in the Electronic Supplement). We set the noise in the envelope templates equal to  $10^{-7}$  m/s (corresponding to the median noise level at the stations used). When calculating the goodness-of-fit for an earthquake we choose the P-arrival at the closest station as the start time  $t_0$  of the envelopes.

## 4 Results and Discussion

In order to evaluate the performance of our proposed algorithm in the scope of EEW, we calculate the mean goodness-of-fit for 10 large Swiss earthquakes (described in the data section) using a wide range of perturbations of the true source parameters, at different times after the event can be first identified. This test assesses the sensitivity of the algorithm to errors in the source parameters. Specifically, we perturb the catalogue magnitude (varying between -1 and 1 in increments of 0.1 magnitude units, with additional gross perturbations of -1.5 and 1.3 magnitude units; the perturbations are corresponding to  $M_{predicted} - M_{true}$ ) and catalogue epicentral location (by distances of 0, 1, 3, 5, 10, 15, 20, 25, 30, 100, and 150 km), and calculate the goodness-of-fit for all possible combinations of these perturbations. We do not perturb the origin time, though origin time er-

rors can have a strong impact on the goodness of fit. Algorithms that do not provide strong constraints on the origin times can be penalised by this metric, and further work is required to address this. We conduct the same analysis for various input window lengths, from windows that end 2s after the data has reached the 1st station, to 40s after, spanning the entire time window from the earliest possible EEW solution using the minimum available data from the fewest stations, to a final automatic location based on the full waveform from the entire network. To perturb the epicentral location, we randomly vary the latitude and longitude of the epicentre in a manner that satisfies the required distance perturbation.

Figure 4 and Figure 5 show the results of all the permuted magnitude-distance pairs for input windows that end 4 and 20 s after the first P-arrival, respectively. Figures S1 (2 s), S2 (3 s), S3 (7 s), and S4 (40 s) in the Electronic Supplement show the same calculations for a wider range of time windows. Our method would provide robust discrimination to larger errors in magnitude and location already at 4 s after the first P-arrival time (Figure 4). Even at this early stage, the method prefers a solution with correct source parameters (i.e. the one with zero perturbation in magnitude and distance). While smaller errors in distance (less than 10 km) and magnitude (less than 0.5 magnitude units) around the true solution also have relatively high fit values (close to or higher than 55), we can see that the fit falls significantly as the perturbation in both magnitude and distance increases. Increasing the window length

### 4 s window

		Distance error (km)										
		0	1	3	5	10	15	20	25	30	100	150
Magnitude error	-1.50	25.46	24.73	23.15	22.03	20.59	14.93	11.76	9.17	5.68	0.00	0.00
	-1.0	38.81	37.79	34.96	33.55	28.38	20.92	14.35	11.80	7.07	0.44	0.00
	-0.9	41.95	40.84	38.87	36.71	29.85	23.40	16.54	10.77	7.65	0.40	0.23
	-0.8	45.14	44.03	40.61	39.02	31.93	24.32	18.12	12.48	7.87	0.00	0.00
	-0.7	48.29	47.08	43.40	42.63	33.83	25.10	19.32	12.87	7.59	0.08	0.00
	-0.6	51.61	49.81	45.94	43.50	38.08	27.81	20.04	14.72	9.60	0.06	0.00
	-0.5	* 55.08	53.01	47.69	44.67	39.38	28.78	18.66	14.99	8.58	0.01	0.00
	-0.4	* 57.90	* 55.05	50.29	48.99	39.83	25.87	21.68	12.83	10.45	0.40	0.00
	-0.3	* 59.82	* 56.79	51.58	49.09	37.76	30.36	22.02	13.03	8.73	0.08	0.18
	-0.2	* 61.28	* 58.10	53.00	49.19	39.96	29.70	19.53	16.89	8.66	0.40	0.04
	-0.1	* 62.29	* 58.92	53.72	50.47	41.97	30.38	21.64	16.53	8.14	0.09	0.03
	0.0	* 62.81	* 59.10	53.88	48.83	41.37	26.79	19.79	13.68	10.95	0.33	0.02
	0.1	* 61.52	* 58.46	* 57.21	49.30	39.60	25.72	21.99	17.23	7.99	0.26	0.00
	0.2	* 59.48	* 57.33	52.48	48.58	37.78	28.22	19.27	14.97	9.22	0.49	0.05
	0.3	* 56.67	* 55.43	* 56.39	47.08	33.60	30.09	21.91	16.96	7.73	0.17	0.02
	0.4	53.39	52.82	51.57	47.64	34.95	25.72	23.46	18.96	8.38	0.15	0.05
	0.5	49.83	50.00	47.53	45.24	32.80	27.01	22.79	13.59	9.74	0.05	0.05
0.6	46.41	47.24	45.42	40.49	34.16	23.43	21.78	14.58	10.19	0.15	0.00	
0.7	42.98	44.56	45.63	39.36	31.07	24.67	19.90	15.12	12.08	0.05	0.20	
0.8	39.85	41.48	40.81	38.15	30.62	25.57	19.92	15.67	9.67	0.01	0.01	
0.9	36.86	38.51	38.05	35.15	30.23	21.79	20.32	17.34	9.61	0.03	0.04	
1.0	33.98	35.69	37.97	29.79	28.62	20.05	18.78	12.96	12.22	0.22	0.00	
1.30	27.04	28.81	29.33	26.29	24.62	18.34	15.51	12.28	8.72	0.03	0.00	

**Figure 4** Average goodness-of-fit for different magnitude-epicentral distance perturbation pairs averaged taken over all 10 events in Table 1 using an input time window ending 4 seconds after the P-arrival at the closest station. The columns and rows show the errors in the source location (km) and magnitude, respectively. The small star in front of a number is used to mark the goodness-of-fit value higher than 55.

### 20 s window

		Distance error (km)										
		0	1	3	5	10	15	20	25	30	100	150
Magnitude error	-1.50	19.56	19.44	19.35	18.62	15.66	13.11	12.10	9.74	8.82	4.41	1.13
	-1.0	32.63	32.24	31.58	30.81	27.16	22.70	19.30	16.89	15.84	7.15	1.82
	-0.9	36.19	35.77	35.35	33.60	30.67	25.40	21.67	19.21	19.49	8.64	3.80
	-0.8	40.11	39.63	39.35	38.38	33.92	28.16	24.44	21.30	19.37	7.74	2.64
	-0.7	44.33	43.88	43.07	42.65	37.15	31.61	26.56	24.07	22.55	11.34	5.46
	-0.6	48.88	48.27	47.73	46.48	40.69	34.81	31.87	26.85	24.79	11.35	4.04
	-0.5	53.70	53.18	52.72	51.87	45.75	39.11	33.15	29.61	26.92	10.15	4.50
	-0.4	* 58.58	* 58.16	* 57.44	* 55.98	49.17	42.06	36.26	32.15	29.42	13.38	5.76
	-0.3	* 63.37	* 62.89	* 62.20	* 60.47	53.55	45.07	38.24	35.39	31.82	13.99	4.41
	-0.2	* 67.15	* 66.65	* 65.68	* 63.88	* 57.12	47.76	39.83	35.17	32.01	14.52	8.45
	-0.1	* 69.23	* 68.75	* 67.75	* 65.26	* 58.41	49.57	41.85	38.89	33.79	14.43	5.09
	0.0	* 70.03	* 69.56	* 68.33	* 65.77	* 58.27	48.64	43.03	39.79	35.42	18.27	9.46
	0.1	* 69.12	* 68.71	* 67.22	* 65.74	* 58.89	50.84	42.46	40.72	37.32	19.53	6.44
	0.2	* 66.46	* 66.14	* 64.68	* 62.93	* 57.11	48.80	44.61	37.27	35.07	19.47	8.56
	0.3	* 62.98	* 62.88	* 61.50	* 60.68	* 55.36	47.19	43.83	40.27	34.04	18.81	9.40
	0.4	* 58.41	* 58.23	* 57.58	* 55.42	51.87	45.51	42.38	39.63	37.13	21.80	8.41
	0.5	53.76	53.70	52.41	52.12	48.79	40.29	39.65	33.03	36.97	21.50	11.13
0.6	49.26	49.22	48.23	47.04	41.82	40.78	34.03	36.72	30.09	19.75	7.35	
0.7	44.82	44.92	44.15	42.91	38.39	37.43	32.13	34.86	31.62	20.76	15.09	
0.8	40.68	40.96	39.62	40.54	36.34	32.68	31.94	30.08	33.02	18.38	10.42	
0.9	37.05	37.19	36.57	36.20	34.41	31.48	30.99	25.97	29.05	19.16	8.40	
1.0	33.67	33.89	34.17	32.21	32.13	26.84	26.90	26.64	27.73	19.71	12.86	
1.30	26.09	26.33	26.64	24.89	24.46	22.29	22.60	19.76	22.00	15.75	9.71	

**Figure 5** Same as Figure 4 for an input time window ending 20 seconds after the first P-arrival at the closest station

(Figure 5) improves the absolute fit for solutions with small magnitude and distance perturbations. Furthermore, there is an improvement in sensitivity to magnitude perturbations (i.e. the fit for larger magnitude errors is decreasing compared to the shorter time window). However, in terms of location error, the sensitivity deteriorates slightly. This can be explained by the inclusion of more distant stations into the goodness-of-fit calculation. Figure S5 in the electronic supplement presents the same results as Figure 5, after 20 s, except

only stations up to 50km from the epicenter are used. For more distant stations, a small change in hypocentral distance does not have a large effect on envelope amplitude. Furthermore, for solutions with significant distance errors, the observed increase in the goodness-of-fit value at longer time windows is also a consequence of the inclusion into the GOF calculation of 1) more distant stations for which the predicted amplitudes are often close to the noise level (Figure S6a), and 2) the stations for which the true and false epicentre can be at a

# Earthquakes

Time after P-arrival at the closest station	2020-11-10 M=3.9 T(1) = 1.8 s T(4)-T(1) = 1.4 s	2020-10-25 M=4.3 T(1) = 1.9 s T(4)-T(1) = 1.3 s	2020-10-25 M=3.6 T(1) = 1.9 s T(4)-T(1) = 1.3 s	2017-07-01 M=4.3 T(1) = 1.2 s T(4)-T(1) = 2.6 s	2017-03-06 M=4.6 T(1) = 1.6 s T(4)-T(1) = 2.4 s	
	1s	0.00	NaN	NaN	60.33	0.09
	2s	77.89	84.12	60.34	92.44	52.61
	3s	56.90	51.34	61.37	25.39	54.44
	4s	59.30	65.76	60.29	75.15	53.56
	5s	68.85	63.08	73.88	53.44	44.63
	7s	69.19	73.95	65.68	67.69	53.68
	9s	68.94	74.36	64.62	69.38	59.33
	12s	64.89	66.28	59.87	66.46	56.84
	15s	74.56	70.48	72.62	69.61	62.83
	19s	74.54	69.65	71.86	73.99	71.85
	25s	76.06	72.56	72.56	75.69	74.43
	30s	75.14	73.95	73.09	74.49	74.34
40s	72.77	71.75	71.34	74.81	75.29	

Time after P-arrival at the closest station	2016-10-24 M=4.1 T(1) = 2.1 s T(4)-T(1) = 1 s	2016-10-07 M=3.8 T(1) = 3.1 s T(4)-T(1) = 2 s	2013-12-27 M=3.7 T(1) = 2.3 s T(4)-T(1) = 0.3 s	2013-12-12 M=4.1 T(1) = 2.4 s T(4)-T(1) = 2.3 s	2013-07-20 M=3.5 T(1) = 1.4 s T(4)-T(1) = 4 s	
	1s	9.98	75.44	38.71	24.74	57.70
	2s	32.95	61.64	75.20	70.38	53.40
	3s	30.35	80.09	70.79	72.29	59.23
	4s	50.68	75.68	68.38	55.37	63.94
	5s	45.65	48.19	66.51	54.54	48.56
	7s	48.01	51.39	63.40	58.03	68.76
	9s	52.82	49.15	67.44	59.87	65.91
	12s	50.50	53.35	60.25	60.04	69.27
	15s	55.52	55.24	70.19	67.18	70.49
	19s	58.13	58.06	70.93	67.06	76.00
	25s	61.11	64.66	72.80	67.67	75.66
	30s	64.21	65.87	72.35	68.95	75.72
40s	64.97	64.60	71.87	70.92	74.90	

**Figure 6** The variation of the goodness-of-fit for the individual earthquakes in Table 1, over time, assuming the correct location and magnitude. The rows show the window length after the P-arrival at the closest station, and the column headers show the date, the magnitude of the earthquake, the travel times for the first station T(1), and the difference between the travel times at the first and the fourth stations T(1)-T(4). The hatched cells show the times when the P-waves would not yet have reached 4 stations - i.e. before an EEW alert could be released. The small star in the right bottom corner of the cell is used to mark the goodness-of-fit value higher than 55.

similar distance (Figure S6b), e.g. a station halfway between the true and false epicentre.

For the purpose of the current study, we consider 55 as the goodness-of-fit threshold which we would use to define a solution acceptable. However, a more in-depth analysis in real-time testing (as discussed later in the text) is required to define a threshold which would minimize false alerts while allowing for selection of good solutions.

Figures S1, S2, S3 and S4, presenting different time windows, show similar patterns as in Figures 4 and 5. However, at very short time windows, the goodness of fit does not always increase with time - at 2 s fit values at and close to the correct solution are higher than at 3 s, 4 s or 7s. This is a consequence of having a smaller number of stations in the goodness-of-fit calculation (for the shorter time windows) which have a strong individual influence on the final goodness-of-fit metric.

Figure 6 summarises the evolution in goodness of fit

over time for the correct or perfect solution (i.e. using the network derived location and magnitude, so distance and magnitude error are zero) for each of the 10 largest individual events. The same general variations seen for the combined events persist for the individual events. At 1 s, solutions are often missing (none of the stations have their amplitudes above the amplitude threshold) or have a very poor fit. Note in the column header, the time after the origin time of the 1st and 4th pick is provided for each event. This time difference is a proxy for the very earliest time an EEW solution could be available using a network-type EEW approach like for VS or FinDer. For the dense Swiss network, this value ranges from 0.3 to 4 s - and in many cases, a first solution would be available only 2 s after the 1st arrival. In Figure 6, shaded cells indicate when the goodness of fit would be computed before a 4-station EEW solution is possible. In the first few seconds, we also observe strong goodness-of-fit varia-

tions for individual earthquakes, which is mostly a consequence of the wrong travel times predicted through the envelope prediction relationship (we did not adapt the travel times to Switzerland). The goodness-of-fit improves for all of the individual earthquakes over time, and for the majority of them converges to a similar value when longer time windows are used. If we take 55 as a goodness-of-fit threshold value we can see that the algorithm would prefer the correct solution from the time the first EEW alert has been issued for 7 events, while for 3 events it would take 9 and 12 s to reach the threshold.

Figures 7 to 10 show the result of the goodness-of-fit for the false alarm origins listed in Table 2. The method again shows good performance, it would allow for false alarm discrimination in practically all cases. The method provides extremely low goodness-of-fit values (mostly zero) for all the examples of quarry blasts causing false alarms except one (Figure 7). The example with the high goodness-of-fit value - just reaching the 55 threshold for some window lengths - actually had the correct location, though the magnitude was overestimated by 0.5 magnitude units, making it by far the 'least wrong' of all the examples. The goodness of fit values over time for these examples are consistent with the previous Figures 4, 5 and S1-S4. Extremely low goodness-of-fit results are also observed for false alarms caused by events close to Swiss borders and for false alarms without a specific event being the cause of the false alarm (both types in Figure 10). The algorithm can also clearly discriminate against the false alarms caused by teleseismic and regional earthquakes (Figures 8 and 9). We can also see that the goodness-of-fit tends to increase with increasing time window length for some of the false alarms. As noted before, this results from the inclusion of more distant stations into the calculation for which the predicted envelope amplitudes are close to the noise level. It should be noted that a goodness-of-fit value of zero was assigned in cases when no stations reached the required threshold level (explained at the beginning of the chapter). The predicted envelopes do not include event type. However, the efficacy of the method on different event types is demonstrated in Figures 7 to 10.

The method is shown to be highly effective, with favourable results observed almost immediately (2 s) after the P-wave arrival at the first station. This suggests our goodness-of-fit metric can be used to select the preferred of multiple EEW solutions in real-time. The method not only ranks the EEW solutions but also provides a measure of their absolute quality, which can be used to decide whether any of the solutions is acceptable for emitting an alert. The goodness-of-fit does increase for all solutions (even very wrong ones) with the increase of the input window length (i.e. adding more stations). This, however, could be tackled by adjusting the goodness-of-fit threshold with the increase of the input window length, or by weighting the stations according to the distance from the (predicted) epicentre.

The algorithm successfully penalises significant errors in both magnitude and location. Since the approach is based on matching the actually observed

ground motions, it allows for the integration of location and magnitude accuracy estimates into a single quality value. Hence, it provides an independent and fair comparison of very different algorithms, including those that produce a point-source solution with those that produce line-source solutions (for which we could use e.g. the Joyner-Boore distance metric). The results also show that the method effectively suppresses false alarms. We expect that this approach, if integrated into real-time monitoring frameworks, will surpass the performance of the traditional metrics that combine simple parameters (e.g. the number of picks, RMS, azimuthal gap, etc.) and hence can replace them.

A challenge with this method is that the background station noise can be above the predicted ground motions, especially when analysing signals from small earthquakes. High background noise can come from anthropogenic sources or indeed sensor noise if the sensor quality is limited, for example from MEMS accelerometers. In these cases, the final goodness-of-fit value can be dominated by the noise rather than the signal. In this study, we simplify the predicted noise modelling by using the median noise level of the stations used in the analysis, which is a reasonable assumption given the overall high quality of the Swiss network. However, for more heterogeneous networks it may be needed to make the noise modelling more station- or sensor-specific.

In actual network operations, we would restrict the station selection to only stations with predicted P-arrivals. However, in our study using perturbed distance and magnitude errors, we could not select the stations based on the predicted P-arrival times as we did not have the difference in origin times for the different distance perturbations. Thus we only select stations close to the real (catalogue) and predicted hypocenter using the previously described amplitude threshold. Applying this selection allows the cross-correlation fit to decrease the influence of noisy stations on the final goodness-of-fit.

Future improvement in the station selection procedure could come from weighting the stations so as to ensure the most relevant stations have the highest influence on the final goodness-of-fit. This could be achieved by 1) weighting the stations according to their epicentral distance which would reduce the effect of distant stations that have the predicted ground motions close to the noise level and, in a reasonably homogeneously spaced network, are usually more numerous than the more important stations near the epicenter; and 2) down-weighting stations located in spatial clusters as to limit the influence of areas with a high density of stations. Weighting, however, could also have a negative effect (e.g. for large location errors, weighting by distance from the predicted epicenter could downweight important stations near the real epicenter) and requires a detailed analysis of the whole network and the individual stations when implementing the algorithm. We expect that adopting a weighting procedure will allow us to reduce the effect of distant stations increasing of overall goodness-of-fit for wrong solutions as can be observed between Figures 4 and 5. This will also allow

	01-07-2022, M(F)=2.9, M(T)=0.9, De=105 km	05-11-2020, M(F)=2.6, M(T)=1.7, De=38 km	01-10-2020, M(F)=2.5, M(T)=2, De=0 km	26-08-2020, M(F)=2.8, M(T)=1.5, De=140 km	12-06-2019, M(F)=2.8, M(T)=1.6, De=46 km
1 s	0.00	0.00	41.15	0.00	0.00
2 s	0.00	0.00	27.97	0.00	0.00
3 s	0.00	0.00	40.03	0.00	0.00
5 s	0.00	0.00	54.65	0.00	0.00
7 s	0.00	0.00	54.81	0.00	0.00
10 s	0.48	0.00	* 55.40	0.00	0.00
13 s	0.00	0.00	* 55.89	0.00	7.36
17 s	2.52	7.88	42.27	0.00	14.58
23 s	3.14	7.58	42.60	3.44	10.05
28 s	2.70	5.55	42.79	4.03	4.97
38 s	2.79	3.98	46.15	11.16	5.04

**Figure 7** The goodness-of-fit for the false alarms in Table 2. The column header shows the date of the event (as a proxy for ID); the false magnitude  $M(F)$ ; the true magnitude  $M(T)$ ; and distance error  $De$  if caused by a real event. The first columns shows the length of the input time window (in seconds) after the first theoretical P-arrival (using the false location). The small star in front of a number is used to mark the goodness-of-fit value higher than 55. The results are grouped according to the source of the false alarm; here, for **false alarms caused by quarry blasts**.

	31-10-2022, M M(F)=2.8, M(T)=5.1, De=916 km	18-12-2021, M(F)=2.6, M(T)=5.4, De=1664 km	23-05-2020, M(F)=2.6, M(T)=5.3, De=1993 km	30-01-2020, M(F)=2.6, M(T)=5.2, De=2042 km	30-03-2019, M(F)=3.1, M(T)=5.3, De=1274 km	12-10-2013, M(F)=3.6, M(T)=6.4, De=1584 km
1 s	0.00	0.00	0.00	0.00	0.00	0.00
2 s	0.00	0.00	0.00	0.00	0.00	0.00
3 s	0.00	0.00	0.00	0.00	0.00	0.00
5 s	0.00	0.00	0.00	0.00	0.00	0.00
7 s	0.00	0.00	0.00	0.00	0.00	0.00
10 s	0.00	0.00	0.00	0.00	0.00	0.00
13 s	17.00	0.00	0.00	0.00	0.00	0.00
17 s	15.88	0.00	0.00	0.00	0.00	15.40
23 s	12.16	0.00	0.00	0.00	0.00	14.33
28 s	10.03	0.00	0.00	0.00	0.00	9.48
38 s	7.93	21.73	0.00	0.00	0.00	0.00

**Figure 8** Same as Fig. 7, for false alarms caused by regional earthquakes in the Mediterranean.

	01-09-2019, M(F)=2.7, M(T)=6.7, De=152°	30-11-2018, M(F)=3.6, M(T)=7.1, De=71°	18-11-2018, M(F)=2.8, M(T)=6.8, De=151°	08-09-2017, M(F)=3.5, M(T)=8.2, De=90°	22-1-2017, M(F)=3.3, M(T)=7.9, De=119°
1 s	0.00	0.00	0.00	0.00	0.00
2 s	0.00	0.00	0.00	0.00	0.00
3 s	0.00	16.60	0.00	0.00	0.00
5 s	0.00	9.81	0.00	0.00	0.00
7 s	0.00	5.80	0.00	0.00	0.00
10 s	0.00	2.98	0.00	0.00	0.00
13 s	0.00	3.45	0.00	3.24	0.00
17 s	0.00	2.79	0.00	5.07	0.00
23 s	0.00	11.62	0.00	7.34	0.00
28 s	0.00	19.23	0.00	6.87	0.00
38 s	0.00	31.87	0.00	5.18	0.00

**Figure 9** Same as Fig. 7, for false alarms caused by teleseisms.

	21-03-2021, M(F)=2.5, M(T)=3.7, De=248 km	25-10-2020, M(F)=2.7, M(T)=3.6, De=115 km	05-07-2019, M(F)=3.2, False triggers from a non- existing event	11-01-2019, M(F)=3.7, False triggers from a non- existing event
1 s	0.00	0.00	0.00	0.00
2 s	0.00	10.39	0.00	0.00
3 s	0.00	10.05	15.41	0.00
5 s	0.00	12.28	0.00	0.00
7 s	0.00	12.42	0.00	0.00
10 s	0.00	16.43	3.87	0.00
13 s	0.00	16.84	2.61	0.00
17 s	0.00	20.02	5.19	4.52
23 s	4.05	22.74	16.40	7.22
28 s	4.09	24.60	15.33	5.72
38 s	4.07	27.25	20.21	10.70

**Figure 10** Same as Fig. 7, for other false alarms. The first 2 are mislocations close to Switzerland from larger regional events, the second 2 are from non-existing events.

us to more precisely select the goodness-of-fit threshold which we would use to accept a solution.

The processing time of the algorithm (on a personal laptop - Lenovo ThinkPad T14 Gen 2a) was on average 0.65 s per earthquake (tested on the 10 Swiss earthquakes) without significant variation when using different window lengths. This means that the processing time is dominated by loading the observed and predicted envelopes from disk - the calculation of the goodness-of-fit took on average 0.003 s when the envelopes were loaded into the memory. The main improvement in the processing time can then be achieved by loading the envelope data faster (e.g. loading only the envelopes from the triggered stations - in the experiment we loaded the envelopes from all the stations).

Our approach is applicable to any monitoring system, though it relies on having an appropriate set of predicted envelopes for the seismicity being monitored. For Switzerland, as described in the Supplement, we used the original envelope prediction relationship developed by Cua (2005) that was developed using data from Southern California, with modifications to adapt it for Switzerland. Direct application of the method to other regions would likely require customising the envelopes for the specific region or accepting a reduced performance in terms of goodness-of-fit values. Furthermore, it is unclear how well the envelope prediction relationships apply to large (bigger than M 6.5) earthquakes, which could affect the goodness-of-fit values for those events. Some preliminary tests on this topic have been done (Yamada and Heaton, 2008), but more extensive testing is required to confirm these results. To make the method more general, our next steps in improving the method will include developing a more general envelope prediction method developed on a global earthquake dataset with a significant representation of large events (ideally uniform across magnitudes).

The tests in this study were not done in real-time, i.e. we did not account for actual station latencies. On the other hand, we were using only the stations from the CH and C4 networks, meaning that more data could be available from other networks. We were also missing

the real-time trigger information and had to rely on an amplitude threshold as a proxy for triggered stations which could allow non-relevant stations to enter the final goodness-of-fit value. Having real-time information about the event origin time (for the correct or false solutions) will actually improve the performance, as it allows us to select stations based on expected P-arrivals, i.e. only those that are relevant. As noted before, a station weighting procedure will be explored to increase the effect of relevant stations on the overall goodness-of-fit. We relied on the travel times calculated using the original envelope prediction relationship, which resulted in wrong start (onset) times for some of the envelopes. Finally, we expect that the errors in timing/signal quality/metadata could strongly affect the results of the method. The test of the influence of these errors on the results of the method will be made during the real-time implementation of the method, where unplanned errors can occur. Given all the unknowns just described, the real-time implementation of the method will also allow us to understand the performance of the method during times of normal (i.e. low magnitude) seismicity. Therefore, real-time testing of our method is necessary to further confirm it as a practical tool for seismic networks and EEW systems which is the crucial next step in the implementation of the algorithm at SED.

## 5 Conclusions

We have developed an algorithm that allows the preferred location and magnitude selection for EEW and real-time seismic processing and can be used to suppress false alarms. The algorithm computes a goodness-of-fit between emerging observed velocity waveform envelopes at multiple stations in a seismic network and those predicted by the given origin and magnitude. Our algorithm has been developed and tested on 10 Swiss earthquakes with magnitudes from 3.5 to 4.6, and on 20 events that caused false alarms inside the Swiss monitoring network. Results in this study suggest the proposed algorithm can operate effectively in EEW systems as well as in routine seismic processing. Strong perfor-

mance is observed for a range of input window lengths, starting from a few seconds after the P-wave arrival at the first station to longer input window lengths, making the algorithm highly suitable for real-time use. The incorporation of the method into a real-time environment brings more challenges beyond just the calculation of the goodness-of-fit. However, the method can bring significant benefits to operational (EEW and earthquake monitoring) systems, justifying the effort needed to implement it. Future improvements will include: improving amplitude fits by re-calibrating the envelope functions using recently collected data, potentially including regionalisation; improving the predicted onset times; and weighting (clusters of) stations (especially at distance).

## Data and code availability

The observed envelope data and the envelope templates of (Cua, 2005, , not-adapted to Switzerland) are available at <https://zenodo.org/records/10037549>, together with the Python code. The station amplification factors, needed for GMM calculations when adapting the predicted envelopes to Switzerland are available at <https://stations.seismo.ethz.ch/en/home/> (ETH Zurich, Swiss Seismological Service, 2015). The earthquake and station metadata are available through the ETHZ dataset in SeisBench (Woollam et al., 2022).

## Acknowledgements

The Editor wishes to thank two anonymous reviewers for their help in evaluating this article. This study was funded through the Real-time Earthquake Risk Reduction for a Resilient Europe 'RISE' project funded from the European Union's Horizon 2020 research and innovation program under grant agreement No. 821115. Opinions expressed in this paper solely reflect the authors' view; the EU is not responsible for any use that may be made of the information it contains. Contributions from FM are possible thanks to the ATTAC (Alerta Temprana para Terremotos en América Central) project funded by the Swiss Agency for Development and Cooperation (SDC).

## Competing interests

There are no competing interests.

## References

- Allen, R. and Melgar, D. Earthquake early warning: Advances, scientific challenges, and societal needs. *Annual Review of Earth and Planetary Sciences*, 47:361–388, 2019. doi: 10.1146/annurev-earth-053018-060457.
- Behr, Y., Clinton, J., Cauzzi, C., Hauksson, E., Jónsdóttir, K., Marius, C., Pinar, A., Salichon, J., and Sokos, E. The Virtual Seismologist in SeisComp3: A new implementation strategy for earthquake early warning algorithms. *Seismological Research Letters*, 87 (2A):363–373, 2016. doi: 10.1785/0220150235.
- Böse, M., Heaton, T., and Hauksson, E. Real-time Finite Fault Rupture Detector (FinDer) for large earthquakes. *Geophysical Journal International*, 191(2):803–812, 2012. doi: 10.1111/j.1365-246X.2012.05657.x.
- Böse, M., Felizardo, C., and Heaton, T. Finite-Fault Rupture Detector (FinDer): Going real-time in Californian ShakeAlert warning system. *Seismological Research Letters*, 86(6):1692–1704, 2015. doi: 10.1785/0220150154.
- Böse, M., Smith, D., Felizardo, C., Meier, M., Heaton, T., and Clinton, J. FinDer v. 2: Improved real-time ground-motion predictions for M2–M9 with seismic finite-source characterization. *Geophysical Journal International*, 212(1):725–742, 2018. doi: 10.1785/0120220183.
- Böse, M., Andrews, J., Hartog, R., and Felizardo, C. Performance and Next-Generation Development of the Finite-Fault Rupture Detector (FinDer) within the United States West Coast ShakeAlert Warning System. *Bulletin of the Seismological Society of America*, 2023. doi: 10.1785/0120220183.
- Cauzzi, C., Edwards, B., Fäh, D., Clinton, J., Wiemer, S., Kästli, P., Cua, G., and Giardini, D. New predictive equations and site amplification estimates for the next-generation Swiss ShakeMaps. *Geophysical Journal International*, 200(1):421–438, 2015. doi: 10.1093/gji/ggu404.
- C.E.R.N. *CERN Seismic Network*. ETH Zurich. Other/Seismic Network, 2016. doi: 10.12686/sed/networks/c4.
- Clinton, J., Zollo, A., Marmureanu, A., Zulfikar, C., and Parolai, S. State-of-the art and future of earthquake early warning in the European region. *Bulletin of Earthquake Engineering*, 14: 2441–2458, 2016. doi: 10.1007/s10518-016-9922-7.
- Cremen, G. and Galasso, C. Earthquake early warning: Recent advances and perspectives. *Earth-Science Reviews*, 205:103184, 2020. doi: 10.1016/j.earscirev.2020.103184.
- Cua, G. *Creating the Virtual Seismologist: developments in ground motion characterization and seismic early warning*. California Institute of Technology, 2005.
- Cua, G. and Heaton, T. The Virtual Seismologist (VS) method: A Bayesian approach to earthquake early warning. *Earthquake early warning systems*, page 97–132, 2007. doi: 10.1007/978-3-540-72241-0\_7.
- Diehl, T., Kästli, P., and Heimers, S. A location quality score - Documentation of the SeisComp3 Implementation for Seattle/Jakarta, Jun 2015. <https://gitlab.seismo.ethz.ch/sed-sc3/evscore/>.
- Edwards, B. and Fäh, D. A Stochastic Ground-Motion Model for Switzerland. *Bulletin of the Seismological Society of America*, 103 (1):78–98,, 2013. doi: 10.1785/0120110331.
- ETH Zurich, Swiss Seismological Service. The Site Characterization Database for Seismic Stations in Switzerland, 2015. doi: 10.12686/sed-stationcharacterizationdb.
- Eurocode 8. Design of structures for earthquake resistance-part 1: general rules, seismic actions and rules for buildings. *Brussels: European Committee for Standardization*, 2005.
- Kohler, M., Smith, D., Andrews, J., Chung, A., Hartog, R., Henson, I., Given, D., Groot, R., and Guiwits, S. Earthquake early warning ShakeAlert 2.0: Public rollout. *Seismological Research Letters*, 91(3):1763–1775, 2020. doi: 10.1785/0220190245.
- Massin, F., Clinton, J., and Böse, M. Status of earthquake early warning in Switzerland. *Frontiers in Earth Science*, 9:707654, 2021. doi: 10.3389/feart.2021.707654.
- Minson, S., Wu, S., Beck, J., and Heaton, T. Combining multiple earthquake models in real time for earthquake early warning. *Bulletin of the Seismological Society of America*, 107(4): 1868–1882, 2017. doi: 10.1785/0120160331.

Swiss Seismological Service At ETH Zurich. National Seismic Networks of Switzerland. *ETH Zürich. Other/Seismic Network*, 1983. doi: 10.12686/SED/NETWORKS/CH.

Woollam, J., Münchmeyer, J., Tilmann, F., Rietbrock, A., Lange, D., Bornstein, T., Diehl, T., Giunchi, C., Haslinger, F., Jozinović, D., and Michelini, A. SeisBench—A toolbox for machine learning in seismology. *Seismological Society of America*, 93(3):1695–1709, 2022. doi: 10.1785/0220210324.

Yamada, M. and Heaton, T. Real-time estimation of fault rupture extent using envelopes of acceleration. *Bulletin of the Seismological Society of America*, 98(2):607–619, 2008. doi: <https://doi.org/10.1785/0120060218>.

The article *Realtime Selection of Optimal Source Parameters Using Ground Motion Envelopes* © 2024 by Dario Jozinović is licensed under CC BY 4.0.